Atom-Based RF Electric Field Metrology: From Self-Calibrated Measurements to Subwavelength and Near-Field Imaging

Christopher L. Holloway, *Fellow, IEEE*, Matthew T. Simons, Joshua A. Gordon, *Senior Member, IEEE*, Perry F. Wilson, *Fellow, IEEE*, Caitlyn M. Cooke, *Student Member, IEEE*, David A. Anderson, *Member, IEEE*, and Georg Raithel

***Abstract*—We discuss a fundamentally new method for electric (E) field strength (V/m) metrology applicable to the near-field. This new approach is significantly different from currently used field measurement techniques in that it is based on the interaction of radio-frequency (RF) E-fields with Rydberg atoms (alkali atoms placed in a glass vapor cell that are excited optically to Rydberg states). The applied RF E-field alters the state of the atoms. The Rydberg atoms act like an RF-to-optical transducer, converting an RF E-field strength to an optical-frequency response. In this new approach, we employ the phenomena of electromagnetically induced transparency (EIT) and Autler-Townes splitting. The RF transition in the four-level atomic system causes a split of the EIT transmission spectrum of a probe laser into two peaks. This splitting is easily measured and is directly proportional to the applied RF E-field amplitude. The significant dipole response of Rydberg atoms enables this technique to make self-calibrating measurements over a large frequency band including 500 MHz to 500 GHz (and possibly up to 1 THz and down to 10s of megahertz). In this paper, we report on our results in the development of this metrology approach, including the first fiber-coupled vapor-cell for E-field measurements. We also discuss key applications, including self-calibrated measurements, millimeter-wave and sub-THz measurements, field mapping, and sub-wavelength and near-field imaging. We show results for mapping the fields inside vapor cells, for measuring the E-field distribution along the surface of a circuit board, and for measuring the near-field at the aperture in a cavity. We also discuss the uncertainties of this measurement technique.**

***Index Terms*—Atom-based metrology, electromagnetically induced transparency (EIT), field sensors and probe, near-field modeling and measurements, subwavelength imaging.**

Manuscript received October 7, 2016; revised November 28, 2016; accepted December 16, 2016. Date of publication January 10, 2017; date of current version January 25, 2017. This work was supported in part by the Defense Advanced Research Projects Agency under the QuASAR Program and in part by the NIST through the Embedded Standards program.

C. L. Holloway, M. T. Simons, J. A. Gordon, and P. F. Wilson are with the Institute of Standards and Technology, U.S. Department of Commerce, Boulder Laboratories, Boulder, CO 80305 USA (e-mail: holloway@boulder.nist.gov; matthew.simons@nist.gov; josh.gordon@nist.gov; pfw@boulder.nist.gov).

C. M. Cooke is with the Department of Electrical Engineering, University of Colorado Boulder, Boulder, CO 80309 USA (e-mail: cccooke7913@gmail.com).

D. A. Anderson is with the Rydberg Technologies, LLC, Ann Arbor, MI 48104 USA (e-mail: dave@rydbergtechnologies.com).

G. Raithel is with the Rydberg Technologies, LLC, Ann Arbor, MI 48104 USA, and also with the Department of Physics, University of Michigan, Ann Arbor, MI 48109 USA (e-mail: graithel@umich.edu).

Color versions of one or more of the figures in this paper are available online at http://ieeexplore.ieee.org.

Digital Object Identifier 10.1109/TEMC.2016.2644616

I. Introduction

ONE of the keys to developing new science and technologies, is to have sound metrology tools and techniques. Whenever possible, we would like these metrology techniques to make absolute measurements of the physical quantity of interest. Furthermore, a stated goal of international metrology organizations, including the National Institute of Standards and Technology (NIST), is to make all measurements directly traceable to the International System of Units (SI). Measurements based on atoms provide such a direct SI traceability path and enable absolute measurements of physical quantities. Measurement standards based on atoms have been used for a number of years for a wide array of measurements; most notable are time (s), frequency (Hz), and length (m). There is a need to extend these atom-based techniques to other physical quantities, such as electric (E) fields. There is also a pressing need to have physically small probes that are not only self-calibrating but can also perform measurements on a small spatial scale (i.e., subwavelength), as well as performing near- and far-field mapping and imaging.

Fundamental to all E-field measurements is having accurately calibrated probes and antennas. To date, calibrated E-field measurements require a complex and indirect traceability path, whereas E-field measurements based on the atom allow a simple and direct traceability path. Existing field probes require a calibration process that is somewhat of a chicken-and-egg dilemma. To calibrate a probe, we must have a known field. But to have a known field, we must have a calibrated probe. In recent work, we have demonstrated a fundamentally new approach for E-field measurements [1]–[6] that can lead to a self-calibrated measurement and has the capability to perform measurements on a fine spatial resolution in both the far-field and near-field.

This new type of measurement technique is based on the excitation of Rydberg atoms. Atoms in highly excited states that have a strong response to radio frequency (RF) E-field are referred to as Rydberg atoms (or Rydberg states). Alkali atoms can be optically excited to such Rydberg states, and then an applied E-field will alter the resonant state of the atoms. Over 50 MHz to 500 GHz, Rydberg atoms have an extremely large E-dipole response ($\wp > 1000ea_0$, where $\wp$ is the dipole moment of the atomic transition, e is the elementary charge, and a_0 is

the Bohr radius) and can act like a transducer, converting an RF E-field strength to an optical-frequency response. The new approach has several potential benefits over existing techniques, including the following:

1) a direct, SI units linked E-field measurement;
2) a self-calibrating measurement due to atomic resonances;
3) expanded bandwidth versus current technologies, allowing measurements from 50 MHz to 500 GHz and possibly up to 1 THz;
4) a technique that is independent of current approaches (allowing for inter comparisons);
5) a very small spatial resolution (optical fiber and chip-scale); and
6) a technique with vastly improved sensitivity and dynamic range over current E-field methods.

This metrology approach will have far-reaching applications, including transferrable E-field standards, new biomedical metrology, traceable calibrations above 110 GHz (currently not available), and subwavelength imaging and field-mapping in both the far-field and near-field. In this paper, we report on our results in the development of this technique and discuss key applications.

II. The Electromagnetically Induced Transparency (EIT) Approach and Experimental Realization

In this section, we review the basic concept of the measurement approach and give calculations for the various atomic physical parameters used in this approach. The approach utilizes electromagnetically induced transparency (EIT) [7]–[9]. The basic concept uses a vapor of alkali atoms (placed in a glass cell, referred to as a "vapor" cell) as the active medium for the RF E-field measurement. Rubidium (^{85}Rb) and cesium (^{133}Cs) are the two atomic species that are typically used in the approach. The EIT technique involves using two lasers, one laser (called a "probe" laser) is used to monitor the optical response of the medium in the vapor cell and a second laser (called a "coupling" laser) is used to establish a coherence in the atomic system. When the RF E-field is applied, it alters the susceptibility (χ) of the atomic vapor seen by the probe laser as it propagates through the vapor cell. By detecting the probe light propagating through the cell, the RF E-field strength can be determined.

A detailed explanation both from an atomic physics viewpoint and from an effective media viewpoint is given in [1]. Here, we will not provide that level of technical detail but will focus on an explanation on how the measurement is performed. The basic concept is that by manipulating alkali atoms with both optical (laser) fields and RF fields, it is possible to cause a laser to transmit through a vapor cell where it would normally be absorbed by the atoms in the vapor cell. To begin a discussion on the concept of how the probe works, refer to Fig. 1. Fig. 1(a) shows one of the experimental setups used in these studies and Fig. 1(b) shows a block diagram of the setup. These experiments include a vapor cell (filled with ^{85}Rb and/or ^{133}Cs atoms), an RF source, a lock-in amplifier (not shown in photo), a photo diode (called the detector in the photo), a probe laser, and a coupling

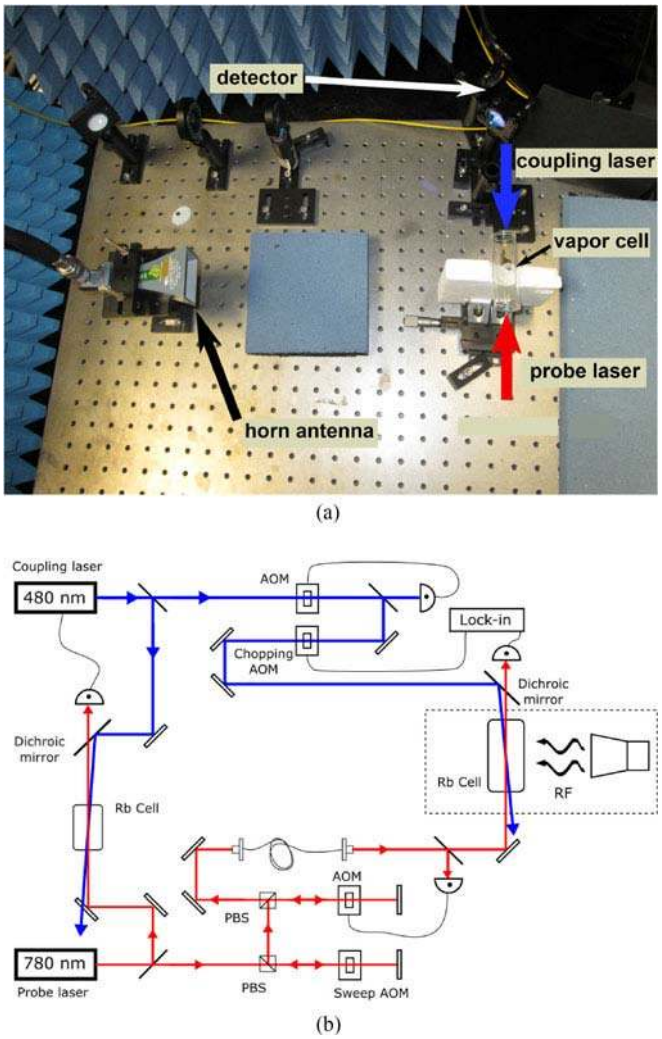

Fig. 1. Experimental setup for E-field measurements using EIT: a) photo of of the setup and (b) block diagram, polarizing beam splitter (PBS) and acousto-optic modulator (AOM).

laser. In the photo the vapor cell in mounted on the optical table. In a Section III, we present a new fiber-coupled vapor cell that allows the probe (i.e., the vapor cell) to be moved off the table.

If the probe laser is tuned to a ground state transition of alkali atoms in a vapor cell, after propagation through the vapor cell the atoms will absorb the light and little power will be detected. For ^{85}Rb this corresponds to a laser of wavelength 780.24 nm, and for ^{133}Cs this corresponds to a laser of wavelength 852.35 nm. The power measured on the detector when the laser is scanned across this wavelength is shown in the bottom curve in Fig. 2(a). In the figure, $\Delta p = \omega_p - \omega_o$; ω_o is the on-resonance angular frequency of the ground state transition and ω_p is the angular frequency of the probe laser. The inverted bell-curve shape (referred to as the Doppler background) is the typical signal one obtains when performing atomic spectroscopy experiments (i.e., the study of the absorption and emission properties of atoms). The minimum in the curve indicates the resonance frequency of the ground state transition of the alkali atom. When the coupling laser is allowed to propagate through the cell (the coupling

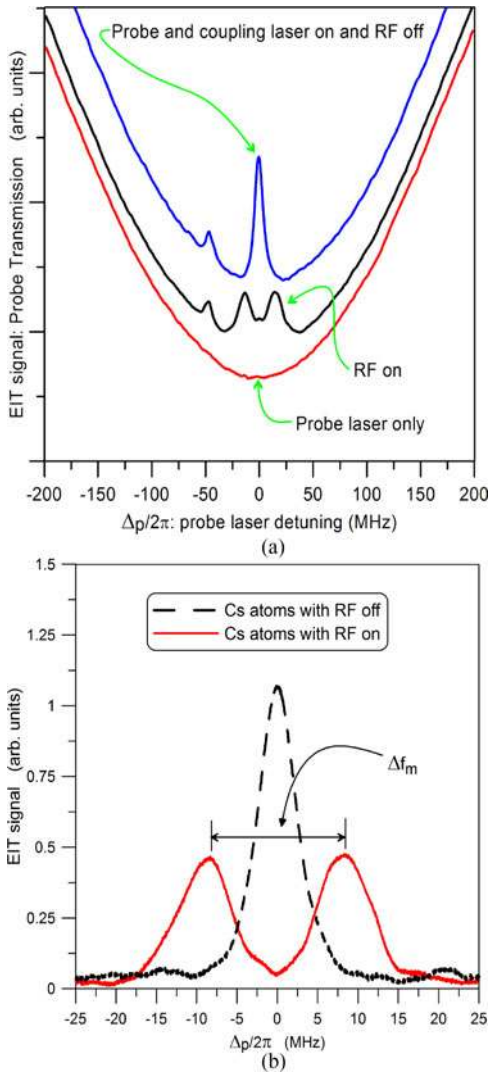

Fig. 2. EIT illustration: (a) with the Doppler background and (b) after the lock-in is used.

laser is counter-propagating on top of the probe laser) the atoms are excited to a higher atomic state. The presence of both the probe and coupling laser cause an interference to the two atomic states, hence allowing the probe laser to pass through the vapor cell with less absorption (an increase in the probe laser transmission). This is the concept of EIT, i.e., a medium that was normally absorbing becomes transparent with the presence of the coupling laser. This is shown in the top curve in Fig. 2(a) (note the wings of all three curves normally would lay on top of one another, but they are shifted here for ease of viewing). Notice at $\Delta_p = 0$, the power on the detector is larger than the Doppler background, i.e., the global inverted bell-shaped behavior. In these experiments, we are interested in the larger peak at $\Delta_p = 0$. The additional peaks to the left of this main peak are related to the atomic structure of the atom (see [3] for details). The wavelength of the coupling laser is chosen judiciously such that the atoms are excited to a very high energy, where an RF source is at a resonant frequency that causes an atomic transition to a nearby state (i.e., an RF atomic transition). This corresponds to a coupling laser wavelength of approximately 480 nm and 510 nm, for ^{85}Rb and ^{133}Cs, respectively. Expressed another way, if the atoms are preconditioned with a probe and coupling laser, then the next atomic transition can be reached with the RF source. When the RF source is turned on, the EIT signal splits into two (this splitting is called Autler-Townes (AT) splitting), see the middle curve in Fig. 2(a). The EIT signal and the splitting can be weak at times. To increase the EIT signal-to-noise, we modulate the coupling-laser amplitude with a 50/50 duty-cycle 30 kHz square wave and detect any resulting modulation of the probe transmission with a lock-in amplifier. This removes the Doppler background and isolates the EIT signal. Fig. 2(b) shows a typical EIT signal from the lock-in amplifier. The splitting of the EIT peak is indicated by Δf_m.

This splitting of the probe laser spectrum is easily measured and is directly proportional to the applied RF E-field amplitude. By measuring the optical frequency difference of this splitting (Δf_m) we get a direct measurement of the RF E-field strength from the following expression [1], [2]:

$$|E| = 2\pi \frac{\hbar}{\wp} \frac{\lambda_p}{\lambda_c} \Delta f_m = 2\pi \frac{\hbar}{\wp} \Delta f_o \tag{1}$$

where $\hbar$ is Planck's constant, $\wp$ is the atomic dipole moment of the RF atomic transition [see (2) below], $\Delta f_o = \frac{\lambda_p}{\lambda_c} \Delta f_m$, and λ_p and λ_c are the wavelengths of the probe and coupling laser, respectively. The λ_p/λ_c ratio is needed to account for the Doppler mismatch of the probe and coupling lasers [8]. The experiments involve changing the power of the RF source (and in turn changing the E-field incident onto the cell) and then measuring the splitting (Δf_m). This measured Δf_m is then used in (1) to obtain the E-field strength. It should be emphasized that this approach only measures the magnitude of the E-field. Since in this approach the atoms only respond to the RF field when the atoms see both the probe and coupling lasers, the location where the field is measured coincides with where the probe and coupling laser overlap.

We consider this type of measurement of the E-field strength a direct SI-traceable, self-calibrated measurement in that it is related to Planck's constant (which will become an SI-defined quantity by standard bodies in the near future) and only requires a frequency measurement (Δf_m, which is quantum linked and can be measured very accurately). The one unknown in the expression is the atomic dipole moment $\wp$ which can be calculated accurately (see [1], [10], [14]).

The dipole moment can be written as [11]:

$$\wp = e\mathcal{A}_{\rm RF}\mathcal{R}_{\rm RF} = e\, a_0\, \mathcal{A}_{\rm RF}\, Q_{\rm RF} \tag{2}$$

where $\mathcal{A}_{\rm RF}$ is the angular part of $\wp$, $\mathcal{R}_{\rm RF}$ is the radial part of $\wp$, and $Q_{\rm RF} = \mathcal{R}_{\rm RF}/a_0$ is the normalized radial part, and a_0 is the Bohr radius ($a_0 = 0.529177 \times 10^{-10}$ m). The angular part $\mathcal{A}_{\rm RF}$ is a function of the polarization of the RF source and is easily calculated, where its value depends on the optical field polarization and the atomic state used [10], [14]. For the cases used in this paper, $\mathcal{A}_{\rm RF} = 0.4899$, other values are given in [14]. The radial part is more involved, requiring one to first numerically solve Schrödinger's equation for the atomic wavefunctions and then a numerical evaluation of the radial overlap integrals

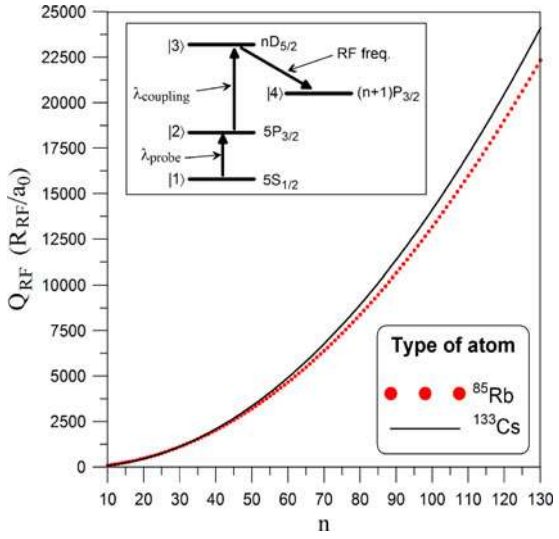

Fig. 3. Calculations of Q_{RF} ($\mathcal{R}_{\mathrm{RF}}/a_0$) for a particular RF atomic transition for ^{85}Rb and ^{133}Cs. The inset is the atomic levels for ^{85}Rb and ^{133}Cs (where n is the principal quantum number and "D" and "P" indicate the angular momentum state of the atoms [15]).

involving the wavefunctions for a set of atomic states (see [1] for details). For a given atomic state or a given atomic transition, these numerical calculations require one to use the quantum defects (along with the Rydberg formula [16]) for the alkali atom of interest. Fig. 3 shows the results of such a calculation for a particular RF atomic transition for both rubidium (^{85}Rb) and cesium (^{133}Cs) atoms. From these results, we see that ^{85}Rb and ^{133}Cs have similar values for $\mathcal{R}_{\mathrm{RF}}$ (or Q_{RF}). These large values of $\mathcal{R}_{\mathrm{RF}}$ for these Rydberg states is what makes this technique beneficial for measuring RF E-fields. Using the best available quantum defects to perform a numerical calculation of $\wp$, it is believed that $\wp$ can be determined to less than 0.1%. This has been verified experimentally in a recent publication [14]. While either of these two atoms can be used, when performing measurements, ^{85}Rb has some advantages at the high RF end of the spectrum and ^{133}Cs has some advantages at the low RF end of the spectrum. The other advantage of ^{133}Cs that may be useful in some situations in that ^{133}Cs has a higher vapor pressure than ^{85}Rb [12], [13]. We used both ^{133}Cs and ^{85}Rb in various experiments presented in this paper.

A single probe has the ability to measure fields ranging from 100s of megahertz to the lower terahertz spectrum. The broadband nature of this technique is due to the large number of possible Rydberg states that can exhibit a large response to an RF source. These states form a discrete set of frequencies that can be measured. The RF source must be tuned to the precise frequency (within a given bandwidth) that corresponds to an atomic transition. The wavelength of the blue coupling laser selects the transition that will respond to the RF source, which defines the frequency that will be measured. While there are a large number of possible atomic states with RF transition frequencies, several of these have small atomic dipole moments. Since the measurement splitting (Δf_m) is directly proportional to the atomic dipole moments, as shown in (1), we want to use RF transitions with large

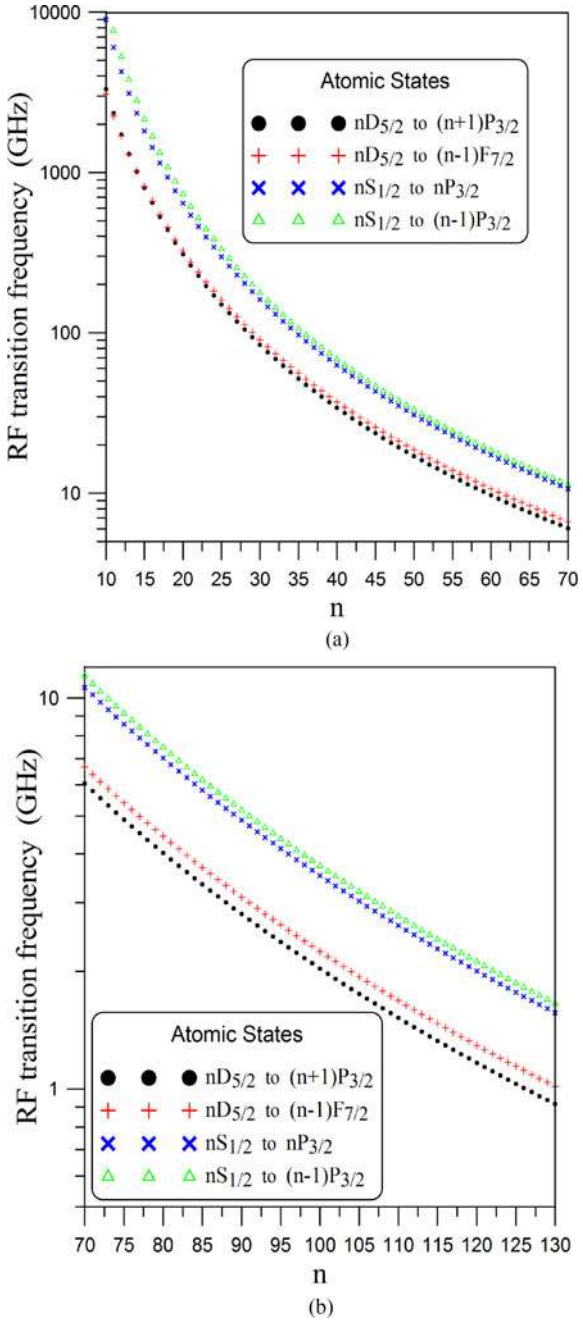

Fig. 4. RF atomic transition frequencies for four atomic transitions, $nD_{5/2} - (n+1)P_{3/2}$, $nD_{5/2} - (n-1)F_{5/2}$, $nS_{1/2} - nP_{3/2}$, and $nS_{1/2} - (n-1)P_{3/2}$: (a) $10 \leq n \leq 70$, and (b) $70 \leq n \leq 130$.

dipole moments. Fig. 4 shows the RF transition frequencies as a function of n (where n is the principal quantum number) for the four atomic transitions that have the largest dipole moments for ^{85}Rb. These four RF transitions correspond to $nD_{5/2} - (n+1)P_{3/2}$, $nD_{5/2} - (n-1)F_{5/2}$, $nS_{1/2} - nP_{3/2}$, and $nS_{1/2} - (n-1)P_{3/2}$ (where "D" and "P" indicate the angular momentum state of the atoms [15]). The results in Fig. 4 were obtained using the Rydberg formula and the quantum defects for ^{85}Rb [16]–[18]. Notice that the frequencies are discrete for a given value of n. While the frequency range that can be

measured using resonant Rydberg transitions is not continuous over the whole spectrum, this figure shows that by using different atomic states it is possible to have small discrete frequency steps. With that said, [14] and [24] illustrate that measurements can be performed over a bandwidth $\pm$ 5% to 10% of a discrete frequency. From the figure, we see that if n ranges from 10 to 130, frequencies ranging from 1 THz to 300 MHz can be measured. A similar set of curves can be generated for ^{133}Cs.

III. Experimental Results

In this section, we describe various measurements using the EIT approach. Section III-A shows examples of RF E-field measurements using a setup similar to that in Fig. 1. Section III-B shows results from scanning the lasers through different vapor cells. In both sections the RF source is either a horn antenna or an open-ended waveguide, and the probe is placed in the far-field. Section III-C shows RF E-field measurements from a fiber-coupled vapor cell. Here different RF sources are used in the measurements: a horn antenna (far-field), a coplanar waveguide (CPW) (near-field), and an aperture in a small transverse electromagnetic (TEM) cell (near-field). For all experiments, we used vapor cells filled with either ^{85}Rb or ^{133}Cs atoms. For ^{85}Rb atoms, the probe is a 780 nm laser which is scanned across the $5S_{1/2}$ – $5P_{3/2}$ transition. We apply a counterpropagating coupling laser (wavelength $\lambda_c \approx 480$ nm, "blue"). For ^{133}Cs atoms, the probe is a 850 nm laser which is scanned across the $6S_{1/2}$ – $6P_{3/2}$ transition and the counterpropagating coupling laser has a wavelength $\lambda_c \approx 510$ nm ("green"). The coupling laser for either atom is tuned to different wavelengths in order to measure the E-field strength at different RF frequencies. The precise wavelength of the coupling laser governs which atomic state is used to measure this E-field strength and the energy difference between these states determines the frequency of the RF field whose strength is measured, as discussed above.

A. E-Field Strength Measurements

Fig. 5 shows the observed splitting of the probe laser transmission spectrum (the EIT signal) for different values of applied RF field. Note that the separation of the two peaks (the splitting) increases with increasing applied E-field strength, as predicted by (1). To obtain these data, a ^{85}Rb atom filled vapor cell is used with the coupling laser tuned to 480.044 nm to couple states $5\mathrm{P}_{3/2}$ and $52\mathrm{D}_{5/2}$, and the RF E-field tuned to 15.095 GHz to couple states $52\mathrm{D}_{5/2}$ and $53\mathrm{P}_{3/2}$. The powers of the probe and coupling lasers are 30 μW and 53 mW, respectively. The probe and coupling lasers are focused to a full-width at half maximum (FWHM) of 75 and 140 μm, respectively.

Fig. 6 shows a set of data for Δf_o (where $\Delta f_0 = \frac{\lambda_p}{\lambda_c}\Delta f_m$) as a function of the square root of the signal generator power (labeled as $\sqrt{P_{SG}}$) for 11.6 GHz. In this data set, a horn antenna is used and connected to a signal generator via a 4-m cable. The horn antenna is 415 mm from the center of the overlapping laser foci at the center of the vapor cell, similar to that shown in Fig. 1(a). We performed the experiment with ^{133}Cs atoms which corresponds to $6S_{1/2} - 6P_{3/2} - 40D_{5/2} - 41P_{3/2}$. We see that the measured Δf_o is linear with respect to $\sqrt{P_{SG}}$ (or

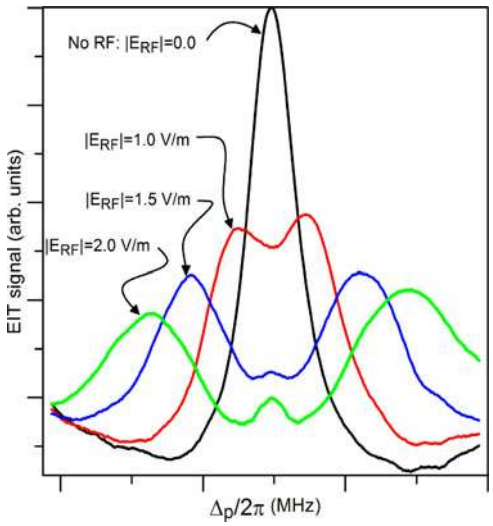

Fig. 5. Experimental data for the EIT signal (i.e., probe laser transmission through the cell) as a function of probe laser detuning Δp. This data set is for a RF signal of 15.095 GHz and corresponds to this following 4-level atomic system: ^{85}Rb for $5S_{1/2} - 5P_{3/2} - 52D_{5/2} - 53P_{3/2}$.

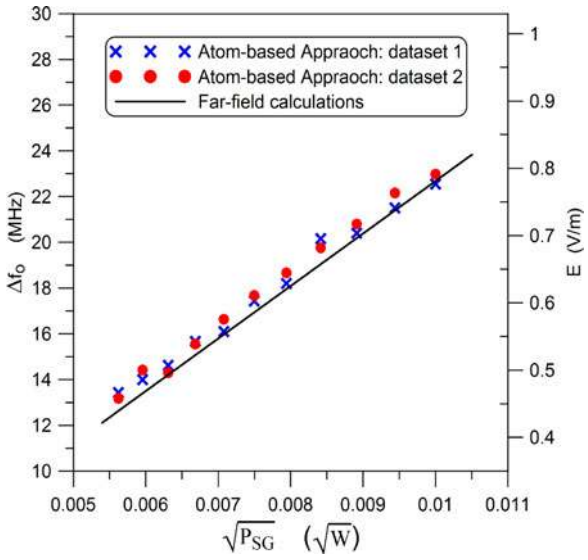

Fig. 6. Measured Δf_o (for ^{133}Cs atoms) and calculated $|E|$ from (1). Also shown are a comparison to far-field calculations. This data set is for a 11.6 GHz field and signal generator power (P_{SG}) corresponding to the power setting on the RF source.

$|E|$), as predicted from (1). Using (1), the E-field is calculated from these measured Δf_o and the results are also shown in Fig. 6 (see the right axis of this plot). In order to validate this technique, we have compared the estimated E-field obtained for this atom-based approach to far-field calculations. Taking into account the distance, the gain of antenna, and the cable losses, the far-field E-field is calculated and the results are also shown in Fig. 6. The good agreement between these results illustrates the validity of the atom-based method.

For additional validations, we perform experiments with both ^{133}Cs and ^{85}Rb atoms to measure the E-field strength at

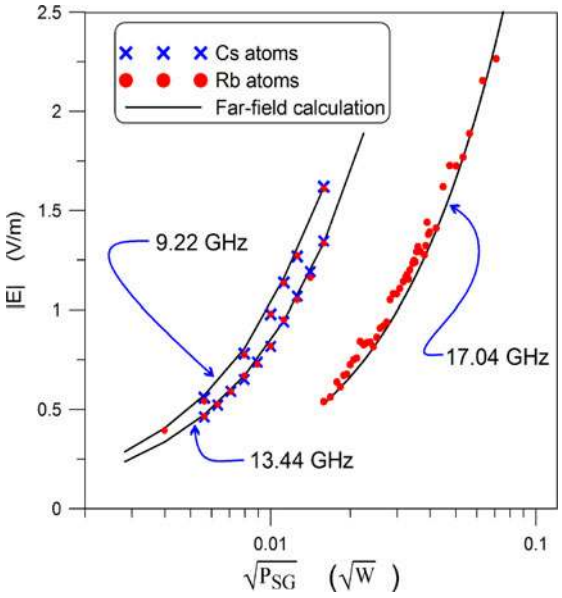

Fig. 7. Measured and far-field calculated $|E|$-field as a function of signal generator power (P_{SG}) for three different frequencies. Note that a log scale is used because the data sets cover different $\sqrt{P_{SG}}$ ranges.

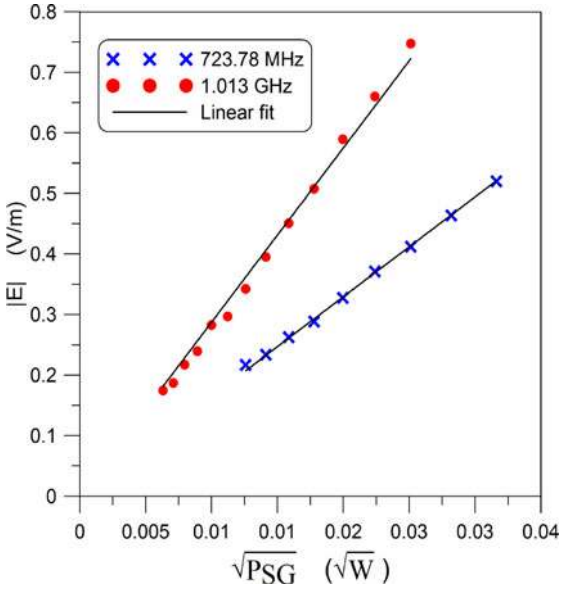

Fig. 8. Measured $|E|$-field as a function of signal generator power (P_{SG}) for 1 GHz and 723 MHz obtained with ^{133}Cs atoms.

9.2 GHz, 13.44 GHz, and 17.04 GHz using a similar experiment setup as that in Fig. 1(a). In two of these experiments, the vapor cell contained both ^{133}Cs and ^{85}Rb atoms. Fig. 7 shows the results for these two-atom experiments. These dual-atom experiments illustrate that the two different atomic species can be used simultaneously to independently measure the same E-field strength. In this figure, we have compared the estimated E-field obtained for this atom-based approach to far-field calculations. The measured E-field strengths obtained for both Cs and Rb show only small deviations from the far-field estimates.

With one experimental setup, it is possible to measure RF E-fields from a few hundred megahertz to 500 GHz (as well as into the THz frequency range and down to 10s of megahertz). We have recently demonstrated measurements for 1 GHz and below. Fig. 8 shows results measured with ^{133}Cs atoms for 1 GHz and 723 MHz for a range of power levels of the signal generator that feeds the cable which, in turn, feeds the horn antenna. Miller, *et al.* [21] have recently performed measurements at 50 MHz and 100 MHz.

New technologies in a variety of industries are emerging that operate at frequencies above 110 GHz and into the THz bands. These include communication systems, biomedical imaging, and atmospherics monitoring, just to name a few. At present, however, there are no established techniques to perform calibrated E-field measurements above 110 GHz. The possibility of performing calibrated measurements above 110 GHz is one of the interesting and possibly, one of the major benefits of this new technique. We are currently expanding this new atom-based technique to perform measurements above 110 GHz. Fig. 9 shows results for four sets of measurements performed from 132 GHz to 203 GHz with ^{85}Rb atoms. These results illustrate the ability to perform "truly" self-calibrated measurements for frequencies above 110 GHz.

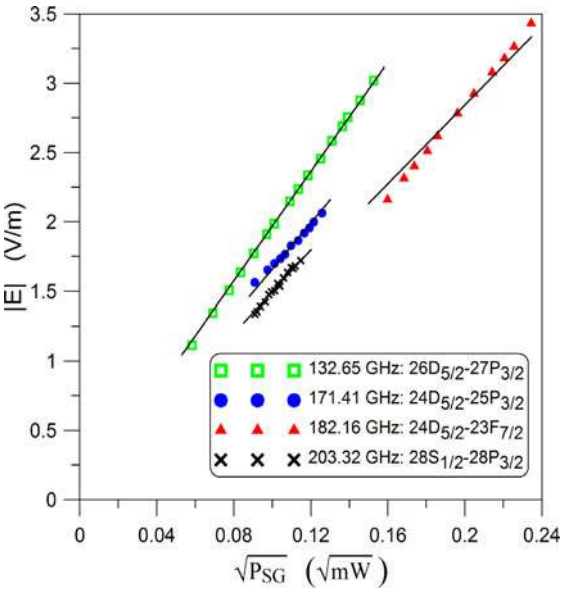

Fig. 9. Measured $|E|$ for frequencies above 110 GHz with ^{85}Rb atoms. Linear fits to the data are shown by lines through the data.

This technique has shown promise for moderate to high field strength measurements [1], [22], [23]. However, it can pose some difficulty for weak field strengths, which can be a problem when performing measurements for frequencies in the upper millimeter-wave and sub-THz bands, where power levels can be low. For weak fields, however, it can be difficult to detect and measure the splitting in the EIT signal. We (and others) are currently researching various techniques for performing higher-sensitivity weak-field measurements (see [2], [24], and [26]). To date, E-field strengths as high as 1000 V/m and as low as 0.8 mV/m have been measured.

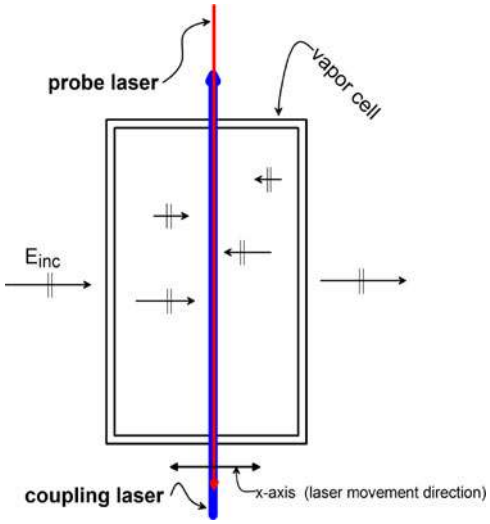

Fig. 10. Illustration of multiinternal wall reflections that cause standing waves inside a glass cell.

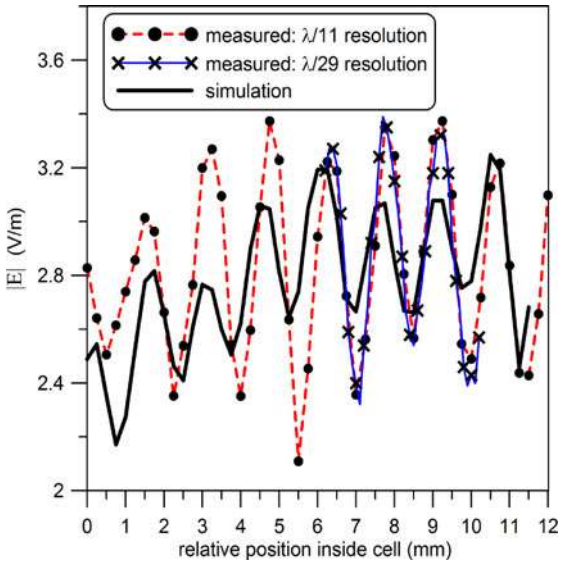

Fig. 11. Measured and simulated results for the field mapping and subwavelength imaging of the E-field distribution in a glass vapor cell. This data set is for 104.77 GHz measured with ^{85}Rb atoms.

B. Subwavelength Imaging and Field Mapping

Because of the nature of these atom-based measurements, the technique is well suited to perform measurements and images on a very small spatial scale. In order for the atom to respond to the RF fields, the atom must simultaneously see the probe laser and the coupling laser, along with the RF field. Hence, the spatial resolution of the method is not governed by the size of the vapor cell holding the atoms, but is governed by the width of the two laser beams. Therefore, the spatial resolution is limited by the optical diffraction limit of the wavelengths of lasers. This is a significant improvement over the measurement resolution achievable by conventional probes.

We can illustrate this by mapping the E-fields inside a glass cell. When an incident field encounters a glass cell (see Fig. 10) a standing wave will develop inside the cell due to internal reflections from the cell walls. We used the atom-based approach to map and image the field distribution inside a cylindrical vapor cell (25-mm diameter and 75-mm long). The lasers are translated across the vapor cell in small steps in x-direction (see Fig. 10). At each step position along x, we measured the splitting of the EIT signal and converted it into an E-field. Fig. 11 shows the field amplitude along the x-axis inside the cell for two different step sizes (corresponding to one-11th and one-29th of a wavelength resolution at 104.77 GHz). These two sets of measurements lie on top of one another, showing that the measurement is repeatable. To obtain these data, the coupling laser is tuned to 482.63 nm to couple states $5P_{3/2}$ and $28D_{5/2}$, and the RF field was tuned to 104.77 GHz to couple states $28D_{5/2}$ and $29P_{3/2}$. The power of the probe and coupling lasers are 120 μW and 22 mW, respectively. The probe and coupling lasers are focused to a FWHM of 75 and 140 μm, respectively. A WR-10 open-ended waveguide, placed in the far-field from the vapor cell, is used as the RF source antenna and is connected to a signal generator. To validate these results, we used the commercial numerical program HFSS (mention of this software is not an endorsement but is only intended to clarify what was done in this paper) to numerically calculate the field distribution inside a cylindrical cell. We used a plane-wave illumination onto the same size vapor cell as the source in the numerical simulations. The numerical results are also shown in Fig. 11. Good qualitative agreement between the numerical results and the measured data is observed. Perfect agreement is difficult because the exact values of both the thickness and permittivity of glass cell are unknown. These data show that we are able to measure and model fields and standing-wave periods much smaller than 1.4 mm (half a wavelength at 104.77 GHz). These results show several standing waves inside the vapor when the cell dimensions are large compared to the RF wavelength, more on this below.

We also measured the field distribution at 15.095 GHz inside a 25-mm x 75-mm cylindrical cell and a 10-mm cubic cell. In these experiments, we measured the field distribution several times and these results are shown in Fig. 12. To obtain these data, the coupling laser is tuned to 480.044 nm to couple states $5P_{3/2}$ and $52D_{5/2}$, and the RF field was tuned to 15.095 GHz to couple states $52D_{5/2}$ and $53P_{3/2}$. The powers of the probe and coupling lasers are 30 μW and 53 mW, respectively. The probe and coupling lasers are focused to a FWHM of 75 and 140 μm, respectively. For the results in Fig. 12, notice that the separation between the maximum and minimum is $\approx \lambda_{\mathrm{RF}}/4$ (where λ_{RF} is the free space wavelength of the RF field and is 19.81 mm), which is expected for a standing wave. The results in this figure were obtained by scanning the cell in 0.1 mm steps, which corresponds to approximately $\lambda/200$ spatial resolution at 15.095 GHz.

In order to verify that the E-field variability inside the cell changes with cell size and shape as indicated by the measured data given in Fig. 12, we performed numerical simulations with HFSS for the E-field distribution inside both a cylindrical and cubic cell. We used plane-wave illumination onto the same vapor cell as the source in the numerical simulations. These numerical

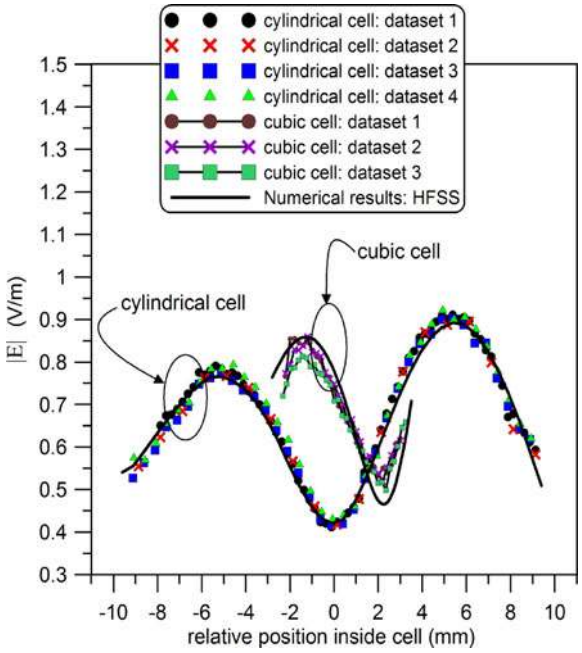

Fig. 12. Repeatability of field mapping measurements for two different size glass vapor cells with ^{85}Rb atoms. The difference data sets correspond to different sets of experiments at different times and these data sets are for 15.095 GHz. The zero position corresponds to the center of the two cells (however, the cubic cell data is shifted by 1 mm to the right such that it can be distinguished from the cylindrical cell data). The lines without symbols show HFSS numerical results for the field distribution inside the two different vapor cells.

simulations for $|E|$ are also shown in Fig. 12. The numerical results agree very well with the measured data. Again, perfect agreement is difficult because the exact values of both the thickness and permittivity of glass cell are unknown.

This figure illustrates two important and interesting points. First, these results show the repeatability of the technique, where we see that the four data sets for the cylindrical cell and the three data sets for the cubic cell lay on top of one another. Second, these results show how the E-field variability inside the cell changes with cell size. As long as the cell cross section is larger than $\approx \lambda_{\mathrm{RF}}/4$, standing waves develop inside the cell (with period of $\approx \lambda_{\mathrm{RF}}/2$). These standing wave effects contribute to the measurement uncertainties of this atom-based technique [1] and [20], see below. This field variability inside the cell can be eliminated or reduced by making the cell cross section smaller than $\approx \lambda_{\mathrm{RF}}/4$ (see [20]).

C. Fiber-Coupled Probe and Near-Field Imaging

Because this technique requires the two lasers (probe and coupling laser) to overlap inside the vapor cell, all measurements to date have required the vapor cell to be confined to an optical bench. We have recently developed the first fiber-coupled vapor cell that allows the probe to be moved off the optical bench. The new probe head is shown in Fig. 13. This probe consists of two optical fibers glued to a 10-mm cubic vapor cell filled with ^{133}Cs. Fig. 14 shows the first set of E-field data from this probe for three different frequencies. For each frequency we performed three sets of data (which are shown in the figure).

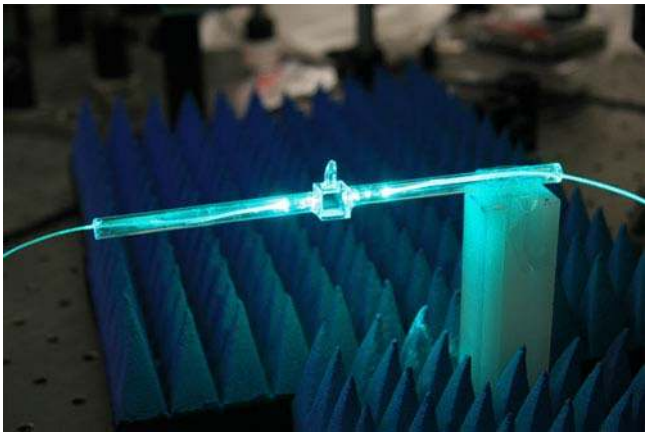

Fig. 13. Photo of first fiber-coupled vapor cell for E-field measurements.

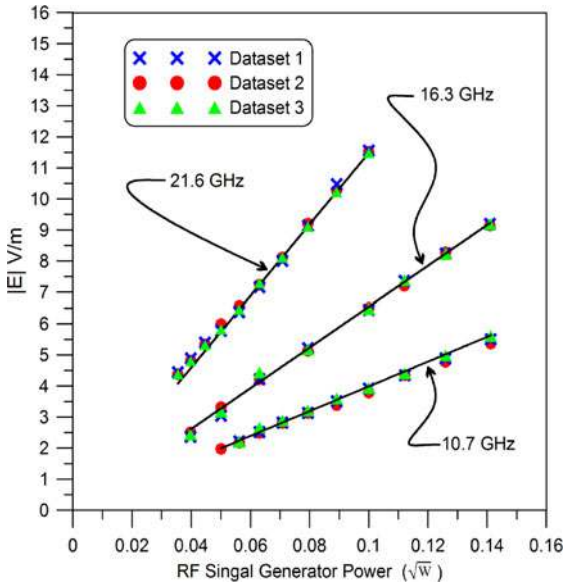

Fig. 14. Measured $|E|$-field as a function of SG power for 10.7 GHz, 16.3 GHz, and 21.6 GHz obtained with the fiber-coupled probe filled with ^{133}Cs atoms.

This illustrates the repeatability of the measurement with this probe head.

In order to demonstrate the near-field measurement/imaging aspects of this new fiber-coupled probe, we performed two sets of near-field experiments. In the first set, we measured the E-field distribution across the surface of a CPW line. The CPW has a center strip of 3 mm, gaps of 2 mm, and a substrate ($\epsilon_r \approx 3.5$) of thickness 1.52 mm. The fiber-coupled probe was scanned across the surface at a height of 6 mm for an input power to the CPW line of -1.24 dBm at 21.6 GHz, see Fig. 15 for the probe positioning. The results for the E-field distribution across the surface of the CPW line are shown in Fig. 16. For a comparison to this measured field distribution, we performed an HFSS simulation of the CPW line. These results are also shown in the figure. We see good qualitative agreement. However, the measured data do show some asymmetry in the field across the CPW gaps with the E-field strength being larger on one side of

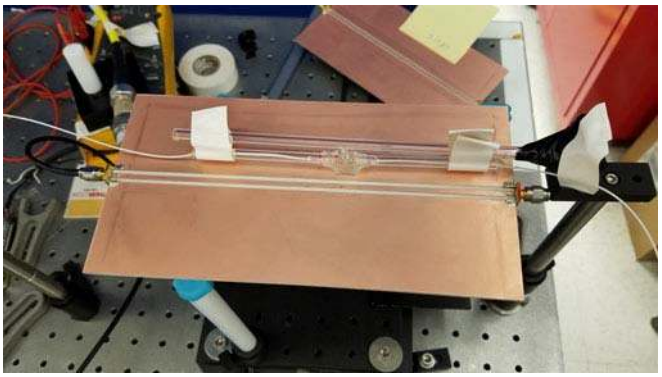

Fig. 15. Photo of CPW line and scan position of the fiber-coupled probe. The CPW line is terminated in a load.

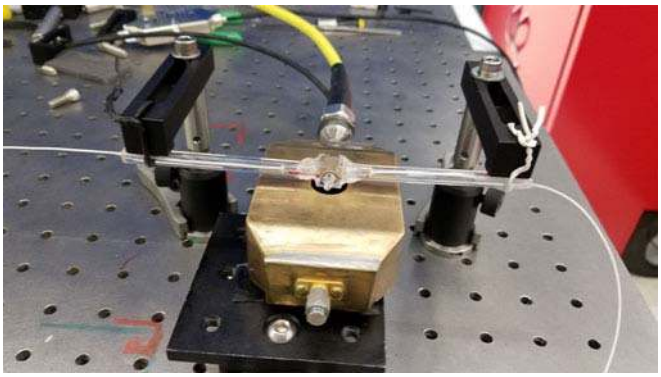

Fig. 17. Photo of TEM cell with aperture and scan position of the fiber-coupled probe.

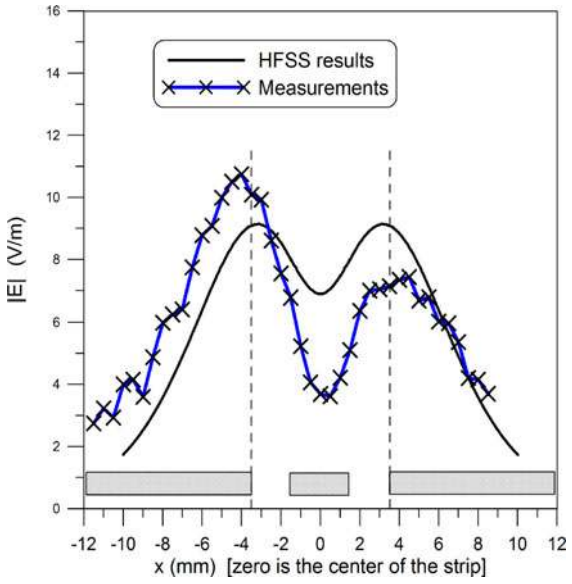

Fig. 16. Measured and simulated $|E|$-field distribution across the surface of the CPW line at 21.6 GHz obtained with the fiber-coupled probe. The frequency corresponds to the ^{133}Cs Rydberg atomic transition $33D_{5/2} - 34P_{3/2}$. We also show the CPW geometry in order to illustrate the gap locations.

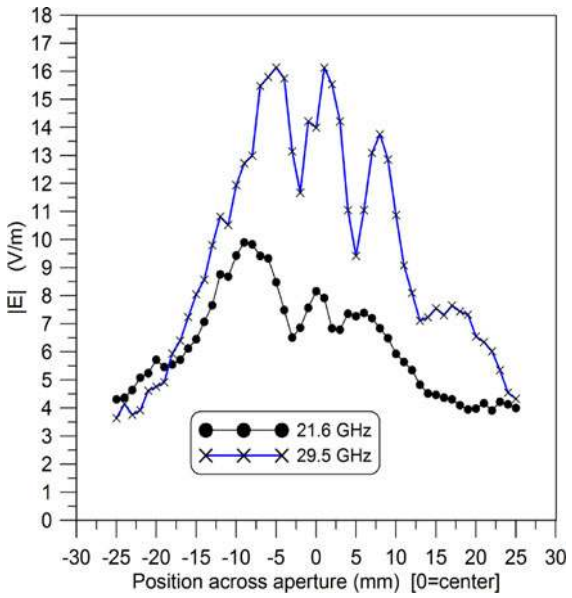

Fig. 18. Measured $|E|$-field as a function of position across the aperture at 21.6 GHz and 29.5 GHz obtained with the fiber-coupled probe. The two frequencies correspond to ^{133}Cs Rydberg atomic transitions of $33D_{5/2} - 34P_{3/2}$ and $30D_{5/2} - 31P_{3/2}$.

the line than the other. We did not use air-bridges in the CPW structure, which are usually used to suppress the unwanted slot-line mode [27]–[29]. The two ground planes must be maintained at the same potential (the purpose of the air-bridges) to prevent this unwanted mode. When the grounds are not at the same potential and the slot-line mode propagates, and the field distribution will be asymmetric across the gaps and becomes larger on one side of the structure. This effect has been independently demonstrated in [30]. Using a magnetic force microscopy technique, they present measured data for the E-field distribution across a CPW line without air-bridges, which shows the same asymmetry behavior. This slot-line mode can be excited with either imperfections in the board or imperfections in the feeding structure. By not using air-bridges, we can measure these asymmetric aspects of unwanted modes caused by these imperfections. Since these imperfections in the CPW line and the feeding structure will not show up in a numerical simulation, these types of measurements allow us to measure asymmetry that cannot be obtained from numerical simulations (illustrating the another benefit of near-field measurements). These results show the capability of near-field imaging across the surface of printed-circuit-board (PCB) structures.

In the next set of experiments, we performed measurements across an aperture located on the side of a small TEM cell. The TEM cell size was 5.5 cm wide, 2.7 cm tall, with an circular aperture of radius 0.75 cm (see Fig. 17). The fiber-coupled probe was scanned across the aperture for a given input power to the TEM cell, see Fig. 17 for the probe positioning. We performed measurements 6 mm from the aperture for the field component transverse to the aperture at 21.6 GHz and 29.5 GHz. Note that the TEM cell is highly multimoded at these two frequencies and the aperture fields cannot readily be calculated; thus, measurements are the best approach to determine the near-fields. The results of the measurements are shown in Fig. 18, illustrating the near-field measurement capability of this approach. This

near-field structure differs from the simpler single-main lobe one expects for an electrically large aperture [25] excited from behind by a simple plane-wave of normal incidence. The field structure incident onto the aperture in our case is much more involved and, as a result, we should expect a different behavior. We should add that an advantage of the vapor-cell near-field probe is that since there is no metal in the probe head, there will be little perturbation in the field caused by the probe itself. However, the mounting structure holding the fibers itself could in principle perturb the field being measured. In future work, we will be investigating how much perturbation the mounting structure causes.

From a near-field imaging aspect, this new measurement technique has the following benefits over other near-field probes:

1) is causes a minimal perturbation in the fields (due to the fact that there is no metal in the probe);
2) it allows for small spatial resolution (subwavelength imaging of the fields);
3) it does not require a calibration;
4) it has expanded frequency bandwidth; and
5) it vastly improves sensitivity and dynamic range.

There are many possible applications of this technique. For example, the sensing volume could be scanned over a printed-circuit-board (PCB) or nanostructure in order to map their fields, as well as other applications where E-field measurements on a small spatial resolution are desired. We are investigating the feasibility of making the vapor cells as small as possible in order to better aid in these subwavelength imaging techniques. In fact, one could envision making arrays of very small vapor cells in order to image an RF field in a two-dimensional space, in effect making an RF camera. We will be investigating these applications in future work.

IV. Uncertainties

For a new measurement method to be accepted by National Metrology Institutes, the accuracy and uncertainties of the approach must be assessed. Knowing the uncertainties of a technique is an important step when establishing a new international measurement standard and is necessary for this method to be accepted as a standard calibration technique. Here, we briefly discuss some of the contributions of the uncertainties.

The uncertainties can be grouped into two different categories: 1) quantum-based uncertainties and 2) RF-based uncertainties. Various quantum-based uncertainties are discussed in [2]. The major contribution to the quantum-based uncertainties is the determination of the atomic dipole moment. The atomic dipole moment is obtained from two numerical calculations (see [1] for details). As discussed above, it is believed that they can be determined to less than 0.1%. This has been verified in [14]. Furthermore, uncertainties of this measurement approach have contributions from statistical and systematic effects in the measurement itself, along with the validity of the linear relationship between the E-field strength and Δf_o as given by (1). This linear relationship can break down under certain conditions involving the EIT signal linewidth which is a function of the power levels of the probe and coupling lasers [31] and [32].

The largest source of measurement uncertainty is RF based, mainly due to the fact that we are using a glass (or dielectric) cell to hold the atoms. As a result, the RF field interacts with the cell itself. The dominant interaction occurs due to standing waves that develop on the inside of the cell, as discussed above. The distribution of the E-fields inside the cell will vary depending on the frequency of the RF E-field and on the size of the cell. This may result in the field inside the cell being different than the incident field (the desired measured quantity), in effect perturbing the RF field by the vapor cell [1], [3], [19], [20]. This is demonstrated in Figs. 11 and 12. This perturbation can be reduced by making the cell as small as possible, and the variability can be eliminated for a cell size below $\lambda/4$ (where λ is the RF wavelength) [20]. Reducing the effects of the vapor cell in these measurements is an area of active research [20]. These results have indicated that for small cell sizes, the variability inside the cell can be less than 2.5%. This corresponds to less than 0.2 dB uncertainties in estimating (and/or measuring) the magnitude of the E-field. With better vapor cell designs, it is believed that this number can be reduced to below 1%. Anechoic chambers or TEM cells are currently used to generate a "known" field in order to calibrate commonly used E-field probes. Due to the uncertainties in this approach, the known field is typically known only to within 5% to 10%. This results in an uncertainty in a field measurement of 0.5to 0.9 dB. Thus, the atom-based technique can be controlled and reduced to be less than the current E-field measurement uncertainties. With that noted, all the effects (along with others) on the uncertainties of the measurement approach are currently being investigated.

V. Conclusion

We have discussed a fundamentally new method for measuring E-fields. This new approach has numerous advantages, as discussed above. Most notable are the self-calibrating, subwavelength measurement, and the near-field imaging aspects. We have also demonstrated the first fiber-coupled vapor cell probe. This technique allows the development of an E-field probe that does not require a calibration, since calibration is an inherent property of the Rydberg atom itself. This technique can also be used to perform subwavelength imaging and near-field mapping over a large range of frequencies. We have demonstrated that the technique can be used to perform calibrated measurements above 110 GHz and below 1 GHz. The applications of such high-resolution spatial imaging capability are numerous, including nanostructure, biological, and near-field imaging, as well as PCB imaging and field mapping.

Acknowledgment

The authors would like to thank Prof. E. F. Kuester and Prof. Z. Popovic at the University of Colorado, Department of Electrical Engineering, Boulder, CO for their useful technical discussions and also to Dr. N. Orloff from NIST for his helpful suggestions on our numerical simulations. The computational results in this work were made possible by the Baker-Jarvis high-performance computer cluster in the Communications Technology Laboratory at NIST.

REFERENCES

[1] C. L. Holloway *et al.*, "Broadband Rydberg atom-based electric-field probe for SI-traceable, self-calibrated measurements," *IEEE Trans. Antenna Propag.*, vol. 62, no. 12, pp. 6169–6182, Dec. 2014.

[2] J. A. Sedlacek, A. Schwettmann, H. Kübler, R. Low, T. Pfau, and J. P. Shaffer, "Microwave electrometry with Rydberg atoms in a vapor cell using bright atomic resonances," *Nature Phys.*, vol. 8, pp. 819–824, 2012.

[3] C. L. Holloway *et al.*, "Sub-wavelength imaging and field mapping via electromagnetically induced transparency and Autler-Townes splitting in Rydberg atoms," *Appl. Phys. Lett.*, vol. 105, 2014, Art. no. 244102.

[4] J. A. Gordon *et al.*, "Millimeter-wave detection via Autler-Townes splitting in rubidium Rydberg atoms," *Appl. Phys. Lett.*, vol. 105, 2014, Art. no. 024104.

[5] J. A. Sedlacek, A. Schwettmann, H. Kübler, and J. P. Shaffer, "Atom-based vector microwave electrometry using rubidium Rydberg atoms in a vapor cell," *Phys. Rev. Lett.*, vol. 111, 2013, Art. no. 063001.

[6] H. Q. Fan, S. Kumar, R. Daschner, H. Kbler, and J. P. Shaffer ,, "Sub-wavelength microwave electric-field imaging using Rydberg atoms inside atomic vapor cells," *Opt. Lett.*, vol. 39, no. 10, pp. 3030–3033, 2014.

[7] M. Fleischhauer, A. Imamoglu, and J. P. Marangos, "Electromagnetically induced transparency: Optics in coherent media," *Rev. Modern Phys.*, vol. 77, pp. 633–673, Apr., 2005.

[8] A. K. Mohapatra, T. R. Jackson, and C. S. Adams, "Coherent optical detection of highly excited Rydberg states using electromagnetically induced transparency," *Phys. Rev. Lett.*, vol. 98, 2007, Art. no. 113003.

[9] K. J. Boller, A. Imamolu, and S. E. Harris, "Observation of electromagnetically induced transparency," *Phys. Rev. Lett.*, vol. 66, no. 20, pp. 2593–2596, May 1991.

[10] I. I. Sobelman, *Atomic Spectra and Radiative Transitions*, 2nd ed. New York, NY, USA: Springer, 1992.

[11] H. J. Metcalf and P. van der Straten, *Laser Cooling and Trapping*. New York, NY, USA: Springer, 1999.

[12] D. A. Steck, "Cesium D line data." [Online]. Available: http://steck.us/alkalidata (revision 2.1.4, Dec. 23, 2010).

[13] D. A. Steck, "Rubidium 85 D line data." [Online]. Available: http://steck.us/alkalidata (revision 2.1.6, Sep. 20, 2013).

[14] M. T. Simons, J. A. Gordon, and C. L. Holloway, "Simultaneous use of Cs and Rb Rydberg atoms for dipole moment assessment and RF electric field measurements via electromagnetically induced transparency," *J. Appl. Phys.*, vol. 102, 2016, Art. no. 123103.

[15] W. Demtröder, *Atoms, Molecules and Phtons: An introduction to Atomic-, Molecular-, and Quantum Physics*, 2nd ed. New York, NY, USA: Springer-Verlag, 2010.

[16] T. F. Gallagher, *Rydberg Atoms*. Cambridge, U.K.: Cambridge Univ. Press, 1994.

[17] W. Li, I. Mourachko, M. W. Noel, and T. F. Gallagher, "Millimeter-wave spectroscopy of cold Rb Rydberg atoms in a magneto-optical trap: Quantum defects of the *ns*, *np*, and *nd* series," *Phys. Rev. A*, vol. 67, 2003, Art. no. 052502.

[18] M. Mack *et al.*, "Measurement of absolute transition frequencies of 87Rb to nS and nD Rydberg states by means of electromagnetically induced transparency," *Phys. Rev. A*, vol. 83, 2011, Art. no. 052515.

[19] C. L. Holloway *et al.*, , "Atom-based RF electric field measurements: An initial investigation of the measurement uncertainties," in *Proc. IEEE Int. Symp. Electromagn. Compat., Europe*, Dresden, Germany, Aug. 2015, pp. 467–472.

[20] H. Fan, S. Kumar, J. Sheng, J. P. Shaffer, C. L. Holloway, and J. A. Gordon, "Effect of vapor cell geometry on Rydberg Atom-based radio-frequency electric field measurements," *Phys. Rev. Appl.*, vol. 4, 2015, Art. no. 044015.

[21] S. A. Miller, D. A. Anderson, and G. Raithel, "Radio-frequency-modulated Rydberg states in a vapor cell," *New J. Phys.*, vol. 18, 2016, Art. no. 053017.

[22] D. A. Anderson *et al.*, "Two-photon microwave transitions and strong-field effects in a room-temperature Rydberg-atom gas," *Phys. Rev. A*, vol. 90, 2014, Art. no. 043419.

[23] D. A. Anderson, S. A. Miller, J. A. Gordon, C. L. Holloway, and G. Raithel, "Optical measurements of strong microwave fields with Rydberg atoms in a vapor cell," *Phys. Rev. Appl.*, vol. 5, 2016, Art. no. 034003.

[24] M. T. Simons, C. L. Holloway, J. A. Gordon, D. A. Anderson, S. Miller, and G. Raithel, "Using frequency detuning to improve the sensitivity of electric field measurements via electromagnetically induced transparency and Autler-Townes splitting in Rydberg atoms," *Appl. Phys. Lett.*, vol. 108, 2016, Art. no. 174101.

[25] C. J. Daly, T. W. Nuteson, and N. A. H. K. Rao, "The spatially averaged electric field in the near feild and far field of a circular aperture," *IEEE Trans. Antennas Propag.*, vol. 51, no. 4, pp. 700–710, Apr., 2003.

[26] S. Kumar, H. Fan, H. Kubler, J. Sheng, and J. P. Shaffer, "Atom-based sensing of weak radio frequency electric fields using homodyne readout," arXiv:1610.09550v1, Oct. 29, 2016.

[27] L. G. Maloratsky, *Integrated Microwave Front-ends With Avionics Applications*. Norwood, MA, USA: Artech House, 2012.

[28] I. Robertson, N. Somjit, and M. Chongcheawchamnan, *Microwave and Millimetre-Wave Design for Wireless Communications*. Hoboken, NJ, USA: Wiley, 2016.

[29] I. Wolf, *Coplanar Microwave Integrated Circuits*. Hoboken, NJ, USA: Wiley, 20o6.

[30] Y. Endo, M. Fukushima, K. Arai, K. Yanagi, Y. Shimada, and M. Yamaguchi, "Measurement of GHz range magnetic field distribution near a coplanar waveguide using a beating field-type magnetic force microscope," *J. Appl. Phys.*, vol. 115, 2014, Art. no. 17D120.

[31] H. Zhang, L. Zhang, L. Wang, S. Bao, J. Zhao, and G. Raithel, "Autler-Townes spectroscopy with interaction-induced dephasing," *Phy. Rev. A.*, vol. 90, 2014, Art. no. 043849.

[32] C. L. Holloway, M. T. Simons, J. A. Gordon, A. Dienstfrey, D. A. Anderson, and G. Raithel, "Investigation of the Linear Relationship Between the Rabi Frequency and AT Splitting as it Relates to Measurement Uncertainties when Using Electromagnetically Induced Transparency for Electric Field Metrology," in preparation.

Christopher L. Holloway (S'86–M'92–SM'04–F'10) received the B.S. degree in engineering from the University of Tennessee at Chattanooga, Chattanooga, TN, USA, and the M.S. and Ph.D. degrees from the University of Colorado at Boulder, Boulder, CO, USA, both in electrical engineering.

During 1992, he was a Research Scientist with Electro Magnetic Applications, Inc., in Lakewood, CO, USA. His responsibilities included theoretical analysis and finite-difference time-domain modeling of various electromagnetic problems. From the fall of 1992 to 1994, he was with the National Center for Atmospheric Research (NCAR), Boulder, CO, USA. While at NCAR his duties included wave propagation modeling, signal processing studies, and radar systems design. From 1994 to 2000, he was with the Institute for Telecommunication Sciences, U.S. Department of Commerce, Boulder, where he was involved in wave propagation studies. Since 2000, he has been with the National Institute of Standards and Technology, Boulder where he works on electromagnetic theory and metrology. He is also on the Graduate Faculty at the University of Colorado Boulder. His research interests include electromagnetic field theory, wave propagation, guided wave structures, remote sensing, numerical methods, metamaterials, measurement techniques, EMC/EMI issues, and atom based metrology.

Dr. Holloway is a member of URSI Commissions A, B, and E. He worked as a Chair for the U.S. Commission A of URSI from 2012 to 2015, and is currently an Associate Editor of the IEEE TRANSACTIONS ON ELECTROMAGNETIC COMPATIBILITY. He was the Chairman for the Technical Committee on Computational Electromagnetics (TC-9) of the IEEE Electromagnetic Compatibility Society from 2000 to 2005, Co-Chair for the Technical Committee on Nano-Technology and Advanced Materials (TC-11) of the IEEE Electromagnetic Compatibility Society from 2006 to 2011, and the IEEE Distinguished Lecturer for the Electromagnetic Compatibility Society from 2004 to 2006.

Matthew T. Simons was born in Fairfax County, VA, USA, on March 29, 1985. He received the B.S. degree from the University of Virginia, Charlottesville, VA, USA, in 2007 and the M.S. and Ph.D. degrees from the College of William & Mary, Williamsburg, VA, USA, in 2009 and 2014, all in physics.

Since graduating in 2014, he has been a Postdoctoral Researcher in the RF Technology Division of the Communications Technology Laboratory, National Institute of Standards and Technology, Boulder, CO, USA, investigating resonant interactions with Rydberg atoms for RF field detection and metrology. His current interests include in laser-atom interactions, quantum optics, and applying atomic and optical physics to problems in RF, mm-wave, and THz technology.

Joshua A. Gordon (M'05–SM'16) received the Doctorate degree in optics and electromagnetics from the College of Optical Sciences, University of Arizona, Tucson, AZ, USA.

He is a Physicist in the Electromagnetics Division at NIST. His current research areas investigate new technologies for electric field measurements which include robotic based antenna metrology systems, optical techniques for antenna alignment, and atom-based electric-field sensing.

Perry F. Wilson (S'78–M'82–SM'93–F'05) received the Ph.D. degree in electrical engineering from the University of Colorado, Boulder, CO, USA, in 1983.

He currently leads the RF Fields Group in the RF Technology Division, National Institute for Standards and Technology, Boulder. His research interests include the application of electromagnetic theory to problems in electromagnetic compatibility and RF field metrology.

Dr. Wilson is a member of U.S. IEC TC77B TAG, the past Editor-in-Chief of the IEEE TRANSACTIONS ON ELECTROMAGNETIC COMPATIBILITY. He received the 2010 IEEE Electromagnetic Compatibility Society Technical Achievement Award, the 2002 IEEE TRANSACTIONS ON ELECTROMAGNETIC COMPATIBILITY Best Paper Award, and the 2007 U.S. Department of Commerce Gold Medal.

Caitlyn M. Cooke (S'16) received the B.S. and M.S. degrees in electrical engineering both from the University of Colorado at Boulder, Boulder, CO, USA, in 2014 and 2016, respectively, and is currently working toward the Ph.D. degree in electrical engineering at the University of Colorado at Boulder.

From 2014 to 2016, she was with NASA Goddard Space Flight Center, Greenbelt, MD, USA, involved with submillimeter-wave radiometers for CubeSats.

Dr. Cooke received the NASA Space Technology Research Fellowship, in 2016, and is continuing research on millimeter-wave monolithic microwave integrated circuits for radiometer front ends.

David A. Anderson (M'16) received the B.S. degree in physics from Northeastern University, Boston, MA, USA, in 2006, the M.S.E. degree in electrical engineering and computer science and the Ph.D. degree in applied physics both from the University of Michigan, Ann Arbor, MI, USA, in 2011 and 2015, respectively.

He is the President of Rydberg Technologies LLC, which he founded in 2015 for research and development of quantum sensing, measurement, and imaging technologies for radio-frequency, microwave, and terahertz fields. His research interests include in experimental atomic physics with a current focus on Rydberg-atom systems for electric and magnetic field sensing, plasma diagnostics, and measurement applications based on Rydberg electromagnetically induced transparency. He is a member of the American Physical Society and IEEE Electromagnetic Compatibility Society.

Georg Raithel received the Diploma in physics from Ludwig Maximilian University of Munich, Munich, Germany, in 1987, the Ph.D. degree in 1990, and the Habilitation degree in 1995 in Physics, from the Ludwig Maximilian University, in Munich. In his Ph.D. degree, he performed spectroscopy of Rydberg atoms in strong magnetic and electric fields.

He is a Professor of physics at the University of Michigan, Ann Arbor, MI, USA, where he teaches undergraduate and graduate-level courses, conducts research and is involved in outreach activities. From 1990 to 1995, he conducted experiments on Rydberg atoms strongly coupled to high-Q microwave cavities. From 1995 to 1997, he was a Feodor-Lynen Fellow of the Alexander von Humboldt Foundation and researched in the atomic physics group at NIST/Gaithersburg on atoms in optical lattices. In 1997, he accepted a position at the University of Michigan. To date, 20 of his graduate students have received Ph.D. degrees. His research covers many-body quantum systems of cold Rydberg atoms. These systems exhibit interesting coherence properties as well as strong electrostatic interactions, high-precision spectroscopy of optically trapped Rydberg atoms, measurement applications of Rydberg atoms, and cold, guided atomic flows and Bose-Einstein condensation.

Dr. Raithel has organized the 2009 through 2014 Michigan Physics Olympiads for Michigan high schools. He was an Associate Chair of Research in the Physics Department, University of Michigan from 2009 to 2013, and Secretary/Treasurer of the DAMOP division of the APS from 2011 to 2014. He is a Fellow of the APS. He has about 100 peer-reviewed publications and has presented at numerous national and international conferences